*International Journal of Minerals, Metallurgy and Materials*
*Volume 26, Number 5, May 2019, Page 573*
**https://doi.org/10.1007/s12613-019-1766-0**

# Formation and thermodynamics of CaS-bearing inclusions during Ca treatment in oil casting steels

*Xue-feng Bai, Yan-hui Sun, Rui-mei Chen, Yi-min Zhang, and Yi-fan Cai*

Collaborative Innovation Center of Steel Technology, University of Science and Technology Beijing, Beijing 100083, China
(Received: 7 December 2018; revised: 21 January 2019; accepted: 24 January 2019)

**Abstract:** Industrial experiments were carried out to investigate the formation of CaS-bearing inclusion during Ca double modification in oil casting steels using polished cross sections and electrolytic extraction. Immediately after Ca addition, the role of newly generated CaS as an intermediate reaction product, which modified the $Al_2O_3$ inclusion into a liquid calcium aluminate, was confirmed. The formation of transient CaS was attributed to the high surface segregation of S at the liquid steel-calcium vapor interface, where a simple site coverage model based upon the Langmuir adsorption equation was established. Moreover, a CaS outer layer surrounding the liquid calcium aluminate was attained mainly in the tundish, which was distributed unevenly on the surface of liquid particles according to the three-dimensional mapping results. The surface of a well-modified calcium aluminate with higher CaO activity and $Al_2O_3$ activity under bulk composition conditions in the tundish acted as a favorable site for the generation of CaS. Additionally, CaS could be precipitated directly onto existing inclusions during solidification of the steel, which led to various morphologies of CaS-bearing inclusions in slabs. Furthermore, the phase transformation of inclusions during solidification was strongly influenced both by the S content and the Ca/S ratio in the tundish via thermodynamics.

**Keywords:** CaS inclusions; Ca treatment; electrolytic extraction; thermodynamics; three-dimensional investigations

## 1. Introduction

Al is one of the most popular deoxidizers used in steels because of its efficient deoxidation power. However, $Al_2O_3$ inclusions, which form as deoxidation products, are detrimental to the castability of molten steel because of their high hardness and high melting point [1–2]. In oil casting steels, $Al_2O_3$ inclusions can give rise to hydrogen-induced cracking, thereby adversely affecting the steels' corrosion resistance [3–4]. Consequently, a Ca treatment method has been established to improve castability and product quality through the modification of solid $Al_2O_3$ into liquid calcium aluminates [5–7]. Nevertheless, stable CaS with a high melting temperature, which usually forms as a result of a high S concentration or excessive modification of Ca treatment, can result in clogging of a submerged entry nozzle [8].

The deoxidation and desulfurization equilibria of liquid iron by Ca in the Fe–Ca–O–S system have been investigated in laboratory-scale and industrial experiments [8–15], which are useful for characterizing CaS formation during the steelmaking process. With respect to the morphology of CaS, oxide–sulfide duplex inclusions with a CaS shell are typically observed during secondary refining. Ye *et al.* [16] proposed that the CaS could be precipitated on the surface of the liquid calcium aluminate as a ring shape because of the liquid calcium aluminate's high sulfide capacity and low $Al_2O_3$ activity. Geldenhuis and Pistorius [17] reported that free CaS was rarely compared with the CaS–$Al_2O_3$–CaO inclusions at different Ca content injections during industrial trials. An unreacted core model of evolution of the CaO–$Al_2O_3$ system into the CaO–$Al_2O_3$–CaS system was also established by Xu *et al.* [18] to explain the formation of oxide–sulfide duplex inclusions during refining.

Nevertheless, a debate regarding the reaction between the CaS as an intermediate reaction phase and the unmodified $Al_2O_3$ still exists. Traditionally, the modification reaction of $Al_2O_3$ has been carried out using dissolved calcium or calcia [19–20]. Several studies have reported that CaS, which forms as a transient phase immediately upon Ca addition and then decreases to disappear, could modify $Al_2O_3$ inclusions to

Corresponding author: Yan-hui Sun E-mail: sunyanhui@metall.ustb.edu.cn

liquid calcium aluminates [21–24]. Verma *et al.* [23] used literature data related to surface segregation to explain the formation of CaS during the transit stage. Ren *et al.* [24] proposed that the formation of CaS in the concave positions of $Al_2O_3$ inclusions is attributable to a lower interfacial free energy. In addition, Ren *et al.* [25] constructed a model of the kinetics during Ca treatment using FactSage macro-processing. Recently, Liu *et al.* [26] further investigated the effect of S on transient evolutions of inclusions during Ca treatment.

For oil casting steels, the precipitation of CaS inclusions during the solidification process is advantageous in terms of preventing the formation of elongated MnS inclusions in the finished products, which is a risk factor for hydrogen-induced cracking and sulfide stress corrosion cracking of steels [4,27–29]. To explain the precipitation of CaS during solidification, the inter dendritic solidification model coupled with the thermodynamic equilibrium model was applied by Holappa *et al.* [30]. Wang *et al.* [31] conducted laboratory experiments through high-temperature confocal scanning laser microscopy to investigate the formation of CaS on $Al_2O_3$–CaO inclusions during the solidification of steels. Moreover, Guo *et al.* [32] calculated the precipitation of CaS-bearing inclusions and investigated their deformation during rolling in the compact strip production (CSP) process. In a study conducted by Xu *et al.* [18], various morphologies of calcium aluminates wrapped with pure CaS or oxide–sulfide duplex inclusion during the CSP process were observed in element maps recorded with an electron probe micro-analyzer, and the plastic deformation region of oxide–sulfide duplex inclusion was further confirmed.

In summary, the presence of CaS-bearing inclusion in oil casting steels increases the complexity of modified products and thus affects the Ca treatment efficiency. Although existing studies recognize the multiple roles of CaS-bearing inclusion during Ca treatment, researchers have yet to systematically examine the formation mechanism of CaS-bearing inclusion on the basis of thermodynamic understanding at each stage after Ca addition in industry operations. In this study, the behaviors of CaS-bearing inclusions during Ca treatment in oil casting steels were investigated by collecting samples at various times after the Ca treatment. Since traditional two-dimensional (2D) investigations limit the accurate chemical analysis of the inclusion surface, electrolytic extraction was also adopted in the present work to obtain a full understanding of the three-dimensional (3D) features of nonmetallic inclusion [33]. In addition, thermodynamic calculations in the current work were carried out with the aid of FactSage 7.0 software [34]. The specific objectives for this work are outlined as follows: (1) characterize CaS-bearing inclusions during Ca modification, with emphasis on detailing intact 3D features of CaS-bearing inclusions; (2) establish the thermodynamics of CaS during the steelmaking process under the stability and non-equilibrium conditions, predict the precipitation of inclusions after the second Ca treatment during solidification, and thereby elucidate the formation mechanism of CaS-bearing inclusions at various stages during Ca double treatment.

## 2. Experimental

### 2.1. Industrial experiments

The industrial tests were executed at the facility of the Pangang Group Co., Ltd. in China; the process flow is exemplified in Fig. 1. During tapping in the basic oxygen furnace (BOF), the slag-stopping process was applied and the high basicity refining slag was added to the melt. At the Ar-blowing station, Al wire was added first for deep deoxidation before Ar-blowing. During the ladle furnace (LF) treatment, the basicity of the refining slag (wt% CaO/wt% $SiO_2$) was controlled at approximately 10.0 for desulfurization. At the end of ladle processing, 400–600 m of Si–Ca wire was fed into the ladle for the modification of $Al_2O_3$ inclusions. During Ruhrstahl-Heraeus (RH) refining, the vacuum treatment duration exceeded 12 min to eliminate the inclusions to the extent possible. Then, 200–300 m of Si–Ca wire was fed again into the ladle. The supplemental Ca through the second Ca addition compensated for the Ca loss during the RH treatment, thereby enhancing the modification effect of inclusions, especially the re-deoxidized products after the first Ca treatment. Furthermore, the Ca retained in the liquid could positively affect the precipitation of MnS inclusion during solidification. During continuous casting, the casting speed in the test was set at 1.4 m/min

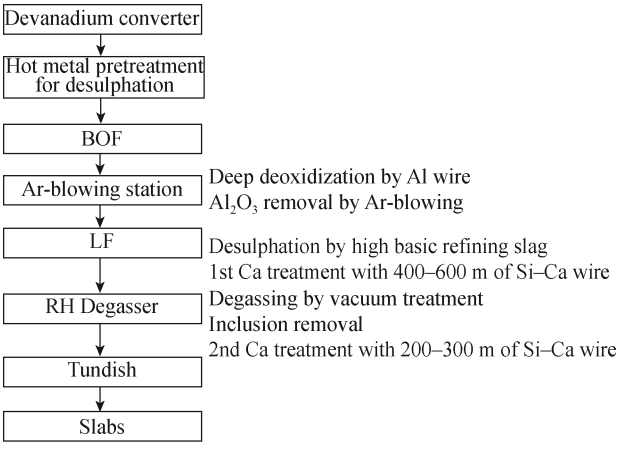


**Fig. 1. Process flow of Ca double treatment.**

and 1.7 m/min. The test samples were obtained from three heats with barrel-type samplers. Specifically, the samples were collected at the Ar-blowing station (A), LF arrival (LF1), prior to LF Ca treatment (LF2), 2 min following the LF Ca treatment (LF3), prior to the RH Ca treatment (RH1), and 2 min following the RH Ca treatment (RH2), in the tundish (T), and in the slabs (S).

### 2.2. Inclusion characterization

For 2D inclusion analysis, the steel samples obtained in the experiments were machined into cylindrical specimens (specimen A, 20 mm in length and 15 mm in diameter). The surface of each specimen was ground with SiC papers up to 2000 grit and subsequently polished with diamond pastes. The 2D characterizations of inclusions, including composition, morphology, structure, and size, were analyzed by scanning electron microscopy (SEM, Zeiss EVO 18th special) in conjunction with energy dispersive spectroscopy (EDS, Nano XFlash detector 5010, Bruker). At least 30 typical inclusions were observed using point and mapping scanning in each sample during 2D inclusion analysis.

For 3D investigations of inclusions in steel, electrolytic extraction, as an effective approach to extract intact inclusions from the steel matrix, was employed in the current work. A specimen (specimen B, Length × width × height = 15 × 15 × 4 mm) was cut from each steel sample for electrolytic extraction. The electrolysis device consisted of a power source, an anode (specimen B), and a cathode (a thin stainless steel loop). In the current study, a 10% AA (10% acetylacetone in volume concentration and 1% tetramethylammonium chloride-methanol in mass concentration) electrolyte was adopted. The electrolysis temperature was set at 0–5°C with the current density at 40–50 $mA \cdot cm^{-2}$. Approximately 0.1 g of metal was dissolved with the electrolytic extraction time set at approximately 4.5–5 h. After electrolytic extraction, the electrolyte was filtered through a polymer membrane with a pore size of 0.4 μm. The filter, after being coated with gold under vacuum conditions, was analyzed for 3D features of inclusions using the SEM (Zeiss Supra 55) combined with EDS (INCA, Oxford).

### 2.3. Bulk chemical analysis

The compositions of steel samples at various sampling locations were analyzed; the results are listed in Table 1. The content of total oxygen (T.O) in each steel sample was analyzed by inert gas fusion-infrared absorptiometry. The content of S in steel samples was determined by the high-frequency induction furnace combustion-infrared absorption method. The dissolved Al ($Al_S$) and Ca contents of steel were analyzed by inductively coupled plasma atomic emission spectrometry (ICP–AES). All of the chemical analyses of steel in this work were carried out at the National Analysis Center for Iron and Steel (NACIS, China).

**Table 1. Compositions of steel samples at various sampling locations** wt%

| Heat No. | Sample No. | Al | O | Ca | S |
|---|---|---|---|---|---|
| 1 | 1-LF1 | 0.110 | 0.0024 | NA | 0.0048 |
| | 1-LF2 | 0.061 | 0.0034 | 0.0015 | 0.0040 |
| | 1-LF3 | 0.027 | 0.0033 | 0.0038 | 0.0019 |
| | 1-RH1 | 0.051 | 0.0046 | 0.0012 | 0.0020 |
| | 1-RH2 | 0.026 | 0.0050 | 0.0034 | 0.0019 |
| | 1-T | 0.026 | 0.0038 | 0.0019 | 0.0030 |
| 2 | 2-LF1 | 0.110 | 0.0024 | NA | 0.0031 |
| | 2-LF2 | 0.045 | 0.0041 | 0.0017 | 0.0017 |
| | 2-LF3 | 0.028 | 0.0067 | 0.0045 | 0.0018 |
| | 2-RH1 | 0.034 | 0.0030 | 0.0016 | 0.0017 |
| | 2-RH2 | 0.025 | 0.0028 | 0.0039 | 0.0018 |
| | 2-T | 0.029 | 0.0034 | 0.0031 | 0.0020 |
| 3 | 3-LF1 | 0.110 | 0.0025 | NA | 0.0047 |
| | 3-LF2 | 0.081 | 0.0028 | 0.0014 | 0.0043 |
| | 3-LF3 | 0.068 | 0.0039 | 0.0051 | 0.0045 |
| | 3-RH1 | 0.067 | 0.0022 | 0.0014 | 0.0031 |
| | 3-RH2 | 0.045 | 0.0037 | 0.0046 | 0.0040 |
| | 3-T | 0.039 | 0.0018 | 0.0023 | 0.0032 |

Note: NA—not analyzed.

## 3. Results and discussion

### 3.1. Characterization of CaS inclusions during Ca treatment

3.1.1. Composition change of inclusions

The composition evolution of inclusions during Ca double addition is presented in Fig. 2. After Ar-blowing, the mean value of $Al_2O_3$ content in the inclusions accounted for approximately 83.69wt%. Subsequently, the CaO content, as well as the MgO content, was gradually increased before the first Ca treatment (as shown in Fig. 1). The source of Mg was the reaction of Al with the MgO-containing refractory material as well as the slag phase, where Ca is provided by the refining slag. After the first Ca addition in LF, the CaS content increased abruptly to approximately 31.64wt% and then decreased to approximately 3.25wt% before the second Ca addition in RH; by contrast, the $Al_2O_3$ content first decreased to approximately 48.84wt% and then increased to 70.62wt%. Furthermore, the CaO content in the inclusions continued to grow during the first Ca treatment. The rapid

changes in both CaS and $Al_2O_3$ contents indicated that the CaS, as an intermediate reaction product, could react with the $Al_2O_3$ inclusions shortly after the Ca addition. Likewise, the mean CaS content increased to 14.46wt% after the second Ca treatment. The $Al_2O_3$ content gradually decreased to 50.11wt%, and the CaO was retained at approximately 29.84wt% in the tundish. Finally, a dramatic increase was observed in the CaS content in the slabs, implying that the CaS phase could be directly precipitated during solidification of steels.

To show the distribution of inclusion compositions during Ca double addition, the inclusion composition data with the mass percentage of (CaO + $Al_2O_3$ + MgO) or (CaO + $Al_2O_3$ + CaS) in inclusions greater than 90wt% were marked in the CaO–$Al_2O_3$–MgO–CaS pseudo-quaternary phase diagram, as shown in Fig. 3. The solid, dashed, and dotted curves in Fig. 3 give the compositions corresponding to

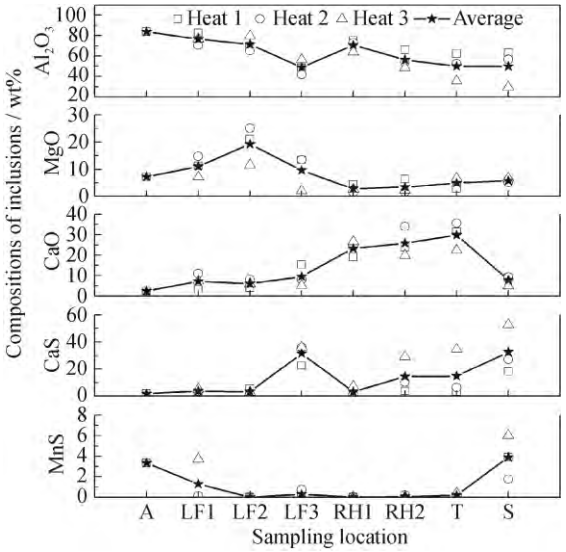


**Fig. 2. Evolution of $Al_2O_3$, MgO, CaO, CaS and MnS contents during Ca treatment.**

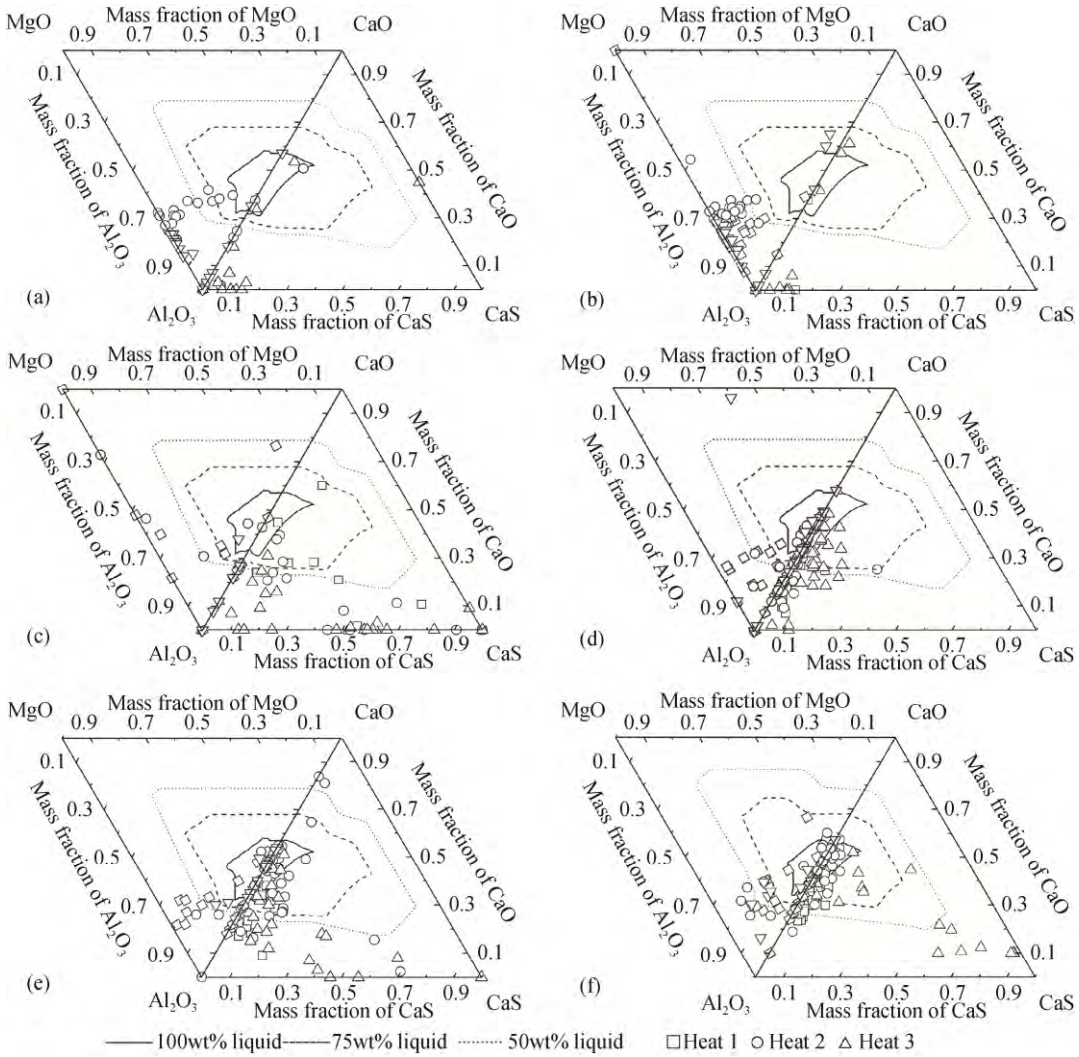


**Fig. 3. Distributions of inclusion compositions in CaO–$Al_2O_3$–MgO–CaS pseudo-quaternary phase diagram during Ca treatment: (a) LF arrival; (b) prior to LF Ca treatment; (c) following LF Ca treatment; (d) prior to RH Ca treatment; (e) following RH Ca treatment; (f) tundish.**

100wt%, 75wt%, and 50wt% liquid at the refining temperature (1600°C, Figs. 3(a)–3(e)) and the tundish temperature (1550°C, Fig. 3(f)), respectively. The liquid boundary used here represents the mass fraction of liquid in the phase compositions, which was calculated using the FactSage 7.0 software.

At the early stages of LF treatment (Figs. 3(a) and 3(b)), $Al_2O_3$ inclusions started to be converted into $Al_2O_3$·MgO spinel and CaO–$Al_2O_3$(–MgO) inclusions with a low CaO content, accompanied by gradual increases of the MgO and CaO contents in the inclusions. Shortly after the LF Ca treatment, the compositions of inclusions were mainly located in two regions, as illustrated in Fig. 3(c). In addition to the calcium aluminate inclusions, other particles were distributed near the CaS–$Al_2O_3$ binary region, accompanied by a substantial increase in the CaS content. However, before the second Ca addition, the compositions of inclusions transferred back to the CaO–$Al_2O_3$ binary region, where approximately half of the inclusions fell within the 50wt% liquid region of the pseudo-quaternary phase diagram, as presented in Fig. 3(d). At the end of the RH vacuum refining, 200–300 m of Si–Ca wire was re-fed into steels to compensate for the Ca loss during RH refining. The compositions of inclusions, accordingly, shifted farther toward the liquid region with some CaS-rich inclusions appearing again, as shown in Fig. 3(e). For samples collected from the tundish (Fig. 3(f)), a majority of the particles entered the 50wt%–100wt% liquid phase zone near the CaO–$Al_2O_3$ binary region through persistent modification reactions in the tundish, which indicated that the Ca treatment had a rewarding modification effect.

3.1.2. Morphology and structure of CaS-bearing inclusions during refining

The 2D mapping of typical CaS–$Al_2O_3$ inclusions observed shortly following Ca addition is illustrated in Fig. 4. The inclusion shown in Fig. 4(a) was observed in 2 min after the first Ca addition. In the 2D elemental map, the areas of Al and O element distributions overlapped, as did the Ca and S distributions. Furthermore, the boundary line between the regions of O and S was not distinct. Apparently, a reaction occurred at the junction of the $Al_2O_3$ and CaS zones. As shown in Fig. 4(b), the zones of concentrated Al and O also overlapped and appeared to be complementary with the zone of concentrated S. However, the Ca element was distributed almost uniformly over the inclusion, indicating that the $Al_2O_3$ phase in the inclusion was partially modified to the $x$CaO·$y$$Al_2O_3$ phase through the further reaction of CaS with the $Al_2O_3$ inclusion. Thus, as the modification reaction proceeded in the melts, the CaS content gradually decreased, whereas the $Al_2O_3$ was utterly modified to a spherical calcium aluminate detected in the tundish (Fig. 4(c)).

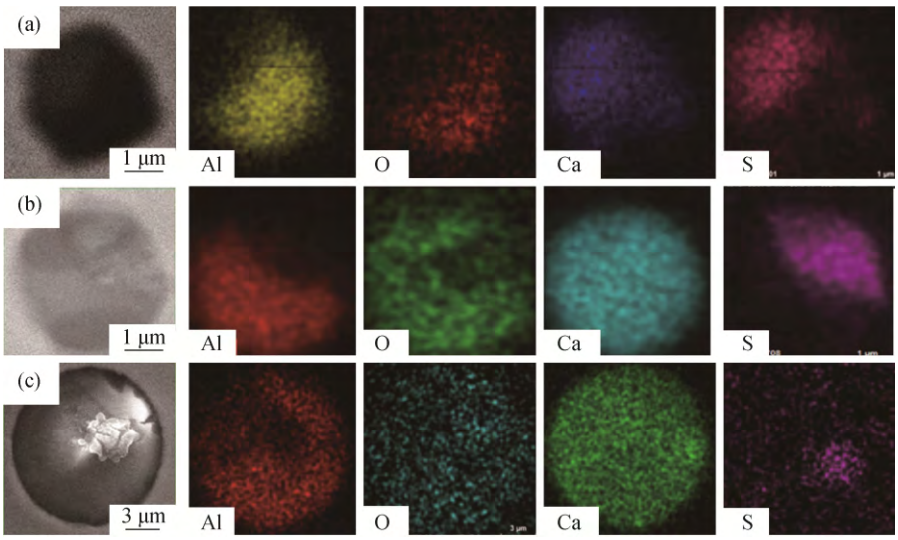


**Fig. 4. 2D composition mappings of typical $Al_2O_3$–CaS inclusions after Ca addition: (a) mapping of dual-phased inclusion of CaS and $Al_2O_3$ observed 2 min after the first Ca addition; (b) mapping of $Al_2O_3$ partially modified by CaS observed in the tundish; (c) mapping of $Al_2O_3$ modified into a spherical liquid inclusion observed in the tundish.**

The 3D composition mapping of this type of CaS-bearing inclusion is presented in Fig. 5. Compared with the cross-sectional analysis, one of great advantages of electrolytic extraction is that the surface-layer compositions can be clearly exhibited by eliminating the interference from the steel matrix. As shown in Fig. 5, the Ca element was not distributed over the whole surface of the particle with an irregular shape but did overlap with the S-concentrated zone. In Fig. 5(a), the region of the $Al_2O_3$ phase was partially wrapped by the CaS phase according to the 3D mapping re-

sults. Additionally, a CaS outer layer could be distributed in the concave position of the alumina inclusion (Fig. 5(b)). When we combined these results with the cross-sectional mapping analysis illustrated in Fig. 4, we concluded that CaS could be formed immediately after Ca addition and adhere to the unmodified $Al_2O_3$.

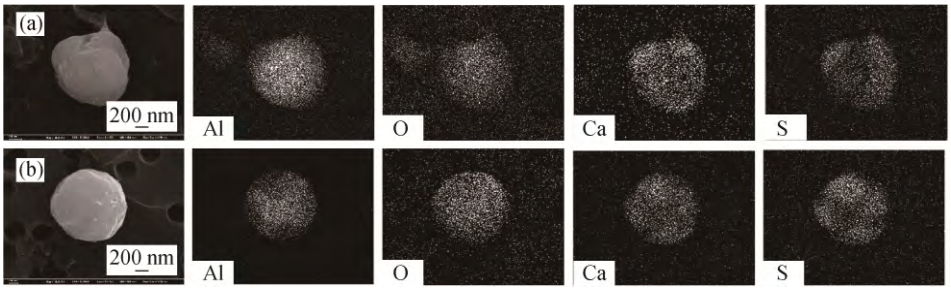


**Fig. 5. 3D EDS-mapping pattern of transient CaS in contact with $Al_2O_3$ shortly after the first Ca treatment: (a) mapping of $Al_2O_3$ partially wrapped by CaS; (b) mapping of CaS distributed in the concave position of $Al_2O_3$.**

The 2D analysis in Fig. 6 reveals another typical type of CaS-bearing inclusion usually observed in the tundish. These CaS-bearing particles were spherical or nearly spherical. The EDS results show that the CaS phase was concentrated on the surface of a liquid calcium aluminate or a spinel–liquid calcium aluminate core as a ring shape. Moreover, the boundary line between the elemental distributions of S and O was also indistinguishable. That is, the outer layer of the inclusions did not consist only of CaS but also a slight amount of the CaO phase, as revealed by 2D mapping.

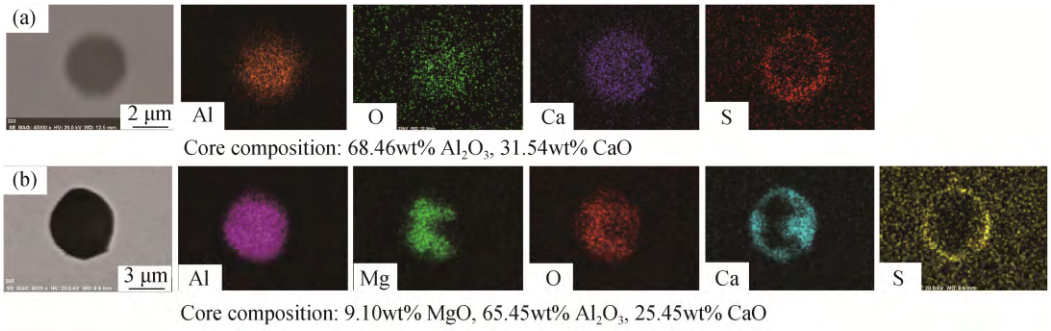


**Fig. 6. 3D mapping analysis of inclusions with a CaS outer layer in the tundish: (a) CaS phase concentrated on the surface of a liquid calcium aluminate core; (b) CaS phase concentrated on the surface of a spinel–liquid calcium aluminate core.**

The 3D mapping results can provide additional information about this type of CaS-bearing inclusion. Fig. 7 shows that the elements Ca, Al, and O were distributed over almost the whole surface of the particle and that their distribution areas were more extensive than that of S. We further deduced that an unclosed ring-shaped CaS layer during cross-sectional observation (Fig. 6(b)) was the result of its uneven distribution. On the basis of the 2D and 3D mapping patterns, the dual-phase inclusions of CaS and CaO–$Al_2O_3$ observed in the tundish are straightforwardly distinguished from the $Al_2O_3$–CaS duplex inclusions found shortly after Ca treatment in this work, which is in agreement with the observations of Verma *et al.* [23].


**Fig. 7. 3D mapping pattern of inclusions with a CaS outer layer in the tundish.**

3.1.3. Morphology and structure of CaS-bearing inclusions in slabs

2D morphologies of typical types of CaS-bearing inclusions in the slabs are presented in Fig. 8. As shown in Figs. 8(a) and 8(b), a ring-shaped CaS layer was distributed surrounding a well-modified or poorly modified CaO–$Al_2O_3$ inclusion core. Figs. 8(c)–8(f) shows typical morphologies of dual-phase inclusions of CaS and $Al_2O_3$, which were also the dominant in-

clusions observed in the slabs, as presented in Fig. 2. In Fig. 8(c), the $Al_2O_3$ particle was almost wrapped by pure CaS, whereas the crescent-shaped CaS directly adhered to $Al_2O_3$, as exhibited in Fig. 8(d). Interestingly, the concave nature of the existing inclusion was also a favorable site for CaS precipitation, as presented in Figs. 8(e) and 8(f). The distribution of Mn was also detected during the mapping analysis and found to be concentrated in the S region, as shown in Figs. 8(c)–8(f).

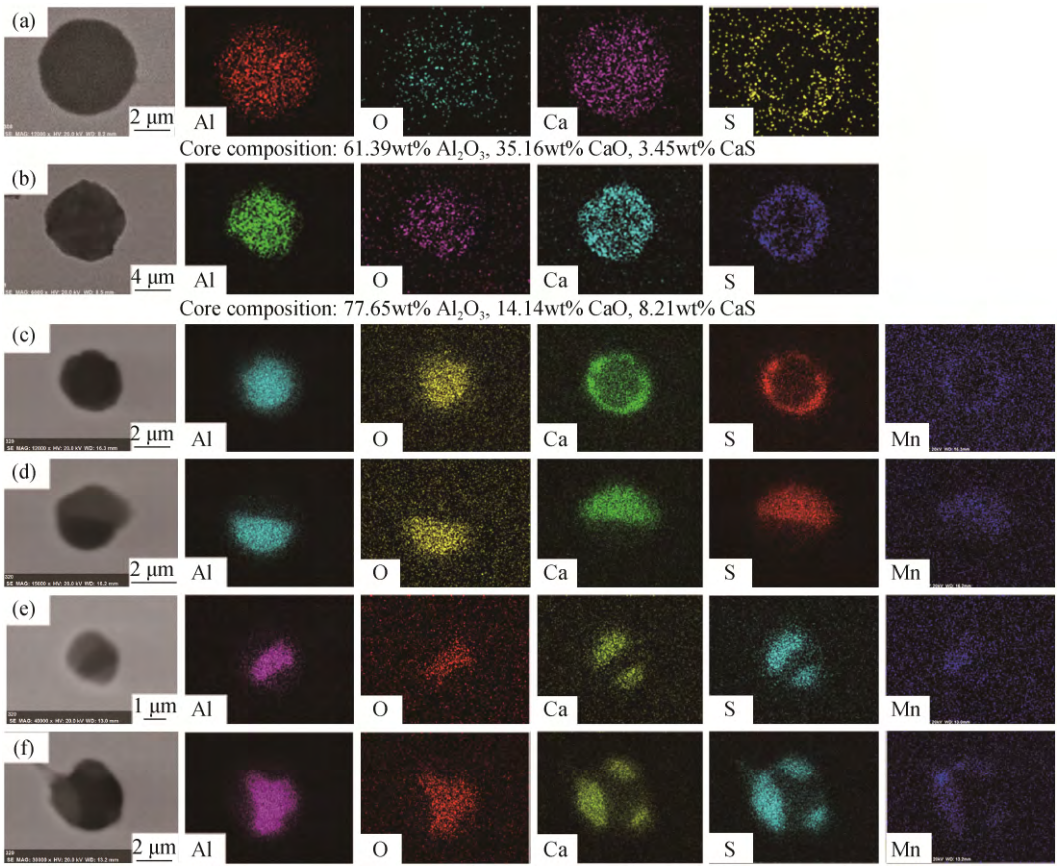


**Fig. 8. 2D composition mapping of CaS-bearing inclusion observed in slabs: (a, b) mapping of $CaO{\cdot}Al_2O_3$ wrapped by CaS; (c) mapping of $Al_2O_3$ wrapped by CaS; (d) mapping of crescent-like CaS adhering to $Al_2O_3$; (e, f) mapping of CaS precipitated in the concave position of $Al_2O_3$.**

Fig. 9 illustrates the 3D morphology of typical CaS–$Al_2O_3$ inclusions observed in slabs. As shown in SEM images, the surface of the outer CaS region with an uneven distribution was relatively smooth compared with the area of $Al_2O_3$. According to the mapping results in Fig. 9(a), the outer layer of the particle was mostly covered by CaS. Fig. 9(b) shows the 3D element mapping images of the dual-phased inclusion of CaS–$Al_2O_3$ with CaS crescent distribution. Based on 3D mapping patterns as shown in Figs. 9(c) and 9(d), the concave position of $Al_2O_3$ provided a favorable site for CaS precipitation. A small amount of Mn was likewise detected in the areas of S and Ca (Figs. 9(b) and 9(d)). In the current work, the phase of MnS, which was predominantly precipitated during cooling of steels according to the results from inclusion composition analysis (Fig. 2), was hardly observed during the high-temperature process. Hence, the large difference between dual-phased inclusions of CaS and $Al_2O_3$ formed during the high-temperature process, and the solidification process is likely due to the presence of MnS. However, some dual-phase inclusions of CaS and $Al_2O_3$ in Fig. 9 appear to contain no MnS. One possible explanation of this difference is control of the MnS precipitation by Ca treatment. In addition, the uneven distribution of MnS at the surface of a particle may be linked to the absence of MnS during 3D inclusion composition analysis. Therefore, further research is required to accurately identify the various CaS-bearing inclusions. Overall, the various morphologies of the CaS-bearing inclusions in the slabs originated from the variety of the existing inclusions during solidification of the steel, which provided the diverse sites for CaS precipitation.

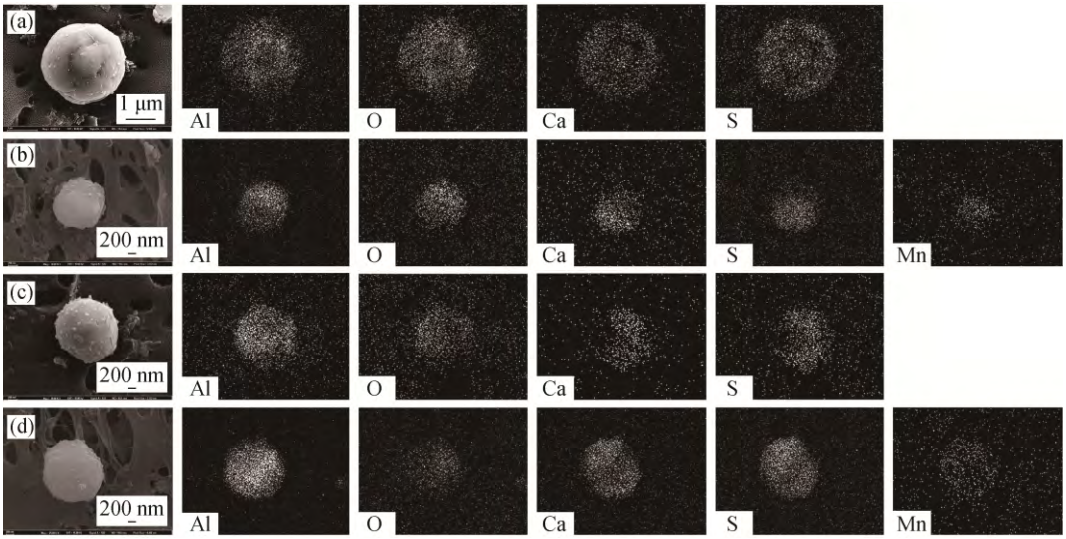


**Fig. 9. 3D element mapping of CaS–$Al_2O_3$ inclusions extracted from slabs: (a) mapping of $Al_2O_3$ wrapped by CaS; (b) mapping of $Al_2O_3$ adhering to CaS; (c, d) mapping of CaS precipitated in the concave position of $Al_2O_3$.**

### 3.2. Thermodynamics of CaS inclusions during Ca treatment

3.2.1. Thermodynamics of stable CaS formation in the molten steel

Fig. 10 exhibits the liquidus projection of the $Al_2O_3$–CaO–CaS system, as calculated by FactSage 7.0 with the FactPS and FToxide databases. One of the Ca treatment objectives in 27CrMoV steels is to improve their castability by modifying the $Al_2O_3$ inclusion into spherical liquid inclusions. However, some weakly modified products, such as $CaO{\cdot}6Al_2O_3$ and $CaO{\cdot}2Al_2O_3$, in combination with CaS formed by Ca overtreatment, can likewise deteriorate the castability because of their high melting points [1,8,35]. Thus, according to Fig. 10, for the liquid region produced in the CaO–$Al_2O_3$–CaO ternary phase diagram at 1600°C, the CaS content should be controlled at less than 8wt% and the CaO content should be maintained between approximately 31wt% and 58wt%.

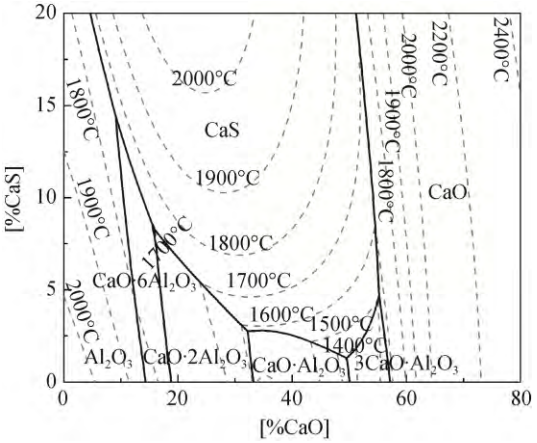


**Fig. 10. Calculated liquidus projection of the $Al_2O_3$–CaO–CaS system.**

Fig. 11 shows the equilibrium relationship between S and Ca for the CaS produced at various O contents in Fe–0.27wt%C–0.3wt%Si–0.45wt%Mn–0.9wt%Cr–0.05wt %Al melt at 1600°C. The calculation was performed using FactSage 7.0 software with the FactPS, FToxid, and FTmisc databases. In Fig. 11, the concentration curve decreases obviously as the T.O content in the melt decreases from 0.0050wt% to 0.0001wt%. Consequently, a high concentration product of Ca and S with low O content enables the easy generation of CaS in molten steel.

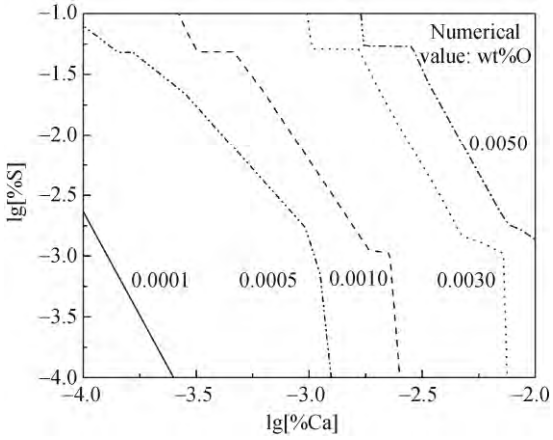


**Fig. 11. Equilibrium relationship between S and Ca for CaS formation at different O contents in oil casting steels at 1600°C.**

The effect of the S content on the equilibrium relationship between O and Ca for the formation of CaO and calcium aluminates is presented in Fig. 12. The blue curves in Fig. 12 represent the zero phase fraction lines of the liquid phase. The equilibrium curves were calculated by the FactSage 7.0 soft-

ware with the FactPS, FToxid, and FTmisc databases in Fe–0.27wt%C–0.3wt%Si–0.45wt%Mn–0.9wt%Cr–0.05wt%Al melt at 1600°C. Overall, the equilibrium relationship between O and Ca shows insignificant changes as the S content increases from 0.0030wt% to 0.0200wt%. With increasing Ca content in 27CrMoV steels, the evolution route of the CaO-bearing inclusions is $CaO{\cdot}6Al_2O_3$ → $CaO{\cdot}2Al_2O_3$ → liquid inclusion → CaO, as indicated in Fig. 12. Furthermore, the range of the liquid curve becomes narrower with decreasing S content, which means that the allowed maximum Ca content for modification can be reduced. Otherwise, the CaO inclusions with a high melting point will be formed in the steel, which is contrary to the goal of Ca treatment.

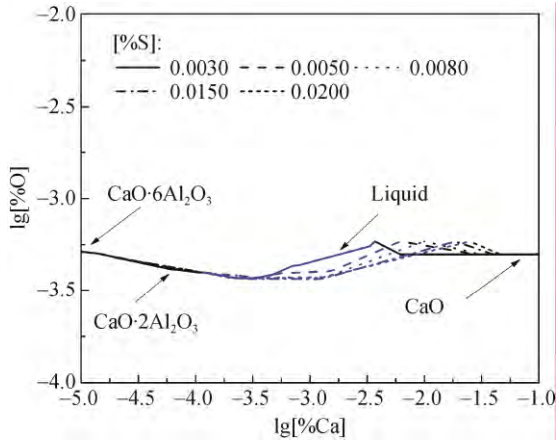


**Fig. 12. Equilibrium relationship between O and Ca for calcia and calcium aluminate formation at different S contents in oil casting steels at 1600°C.**

The stability diagram of inclusions in the Fe–0.27wt%C–0.3wt%Si–0.45wt%Mn–0.9wt%Cr–0.003wt%S–Al–Ca–O melt at 1600°C was calculated using FactSage 7.0 with the FactPS, FToxid, and FTmisc databases, as shown in Fig. 13. The numbers adjacent to each line are the equilibrium O contents in the melts. Fig. 13 shows that the trajectory of inclusions in oil casting steels is $Al_2O_3$ → $CaO{\cdot}6Al_2O_3$ → $CaO{\cdot}2Al_2O_3$ → liquid inclusions with increasing Ca content at 1600°C. $CaO{\cdot}6Al_2O_3$ and $CaO{\cdot}2Al_2O_3$ have been demonstrated to be the primary inclusions that adversely affect the castability of the Al-killed steels [1,35]. Therefore, the Ca content should be carefully adjusted within an appropriate range. Unfortunately, the stability diagram in Fig. 13 could predict the presence of inclusions only after the equilibrium of the reactions and would have failed to explain the formation of CaS during the transient stage following Ca addition.

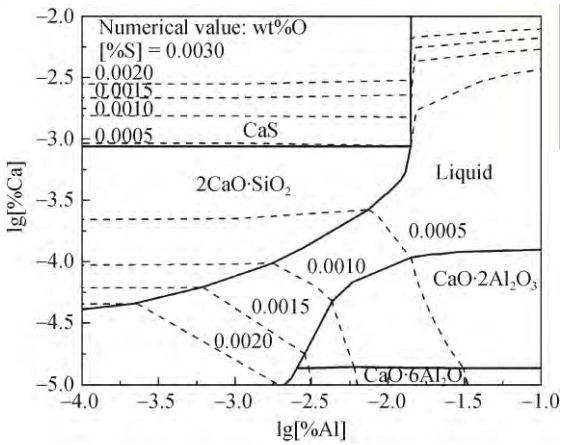


**Fig. 13. Calculated stability diagram of inclusions in Fe–0.27wt%C–0.3wt%Si–0.45wt%Mn–0.9wt%Cr–0.003wt%S–Al–Ca–O melt at 1600°C.**

3.2.2. Thermodynamics for transient CaS formation after Ca treatment

Complex reactions including melting, vaporization, and dissolution of Ca itself, in addition to its reactions with O, S, and Al occur almost simultaneously and constitute a non-equilibrium thermodynamic system in the melts. Further complicating the issue, the Ca vapor and dissolved Ca contents cannot be quantified because of the limited measurements. Therefore, the equilibrium calculations are not suitable for the prediction of inclusion behavior during the transient stage.

In the molten steel, adsorption of strong surface-active elements such as O and S occurs readily at the gas–liquid metal interface, such as decarburization and nitrogen removal [36]. Likewise, immediately after Ca addition, the surface of the Ca vapor bubbles may be an advantageous site for segregation of S and O. In the current work, a Langmuir-type adsorption isotherm was introduced to describe the surface coverages of S and O at the interface between liquid steel and Ca vapor. For the calculation, the following assumptions were made: (1) the surface-active elements of O and S adsorb onto the same site at the liquid–gas interface; (2) the surface coverages of O and S on the site are in the monolayer approximation; and (3) the adsorption reactions occur only on the remaining vacant sites at the interface.

In cases with more than one ideally adsorbing interfering solute, the Langmuir adsorption equation can be expressed as follows [36]:

$$\frac{\theta_i}{1-\sum_j \theta_j} = K_i \alpha_{\%,i} \tag{1}$$

where $K_i$ denotes the adsorption coefficient of interfering solute $i$; $\theta_i$ and $\theta_j$ represent the fractions of sites covered by

interfering solute $i$ and $j$, respectively; and $\alpha_{\%,i}$ denotes the thermodynamic activity of element $i$ relative to the 1wt% standard state.

Fig. 14 shows the surface coverage of the liquid steel by S and O. In Fig. 14, the blue and black curves represent the surface coverage of S and O, respectively, which were calculated according to Eq. (1) with the help of the FactSage software. The adsorption coefficients in the work of Verma *et al.* [23] and those in the present study were both estimated from nitrogen–steel reaction kinetics. Notably, the effects of different pressures on the rate of desorption are not negligible. According to Ban-ya's analysis [37], the values of $K_S$ and $K_O$ at 101325 Pa were 130 and 300 at 1600°C, respectively. In contrast, some researchers [38–40] reported substantially different behaviors at low pressures, where the values of $K_S$ and $K_O$ at pressures of 13.33 to 1599.87 Pa were 63.4 and 161, respectively, were reported by Harashima *et al.* [39]. Thus, the values of $K_S$ and $K_O$ at both high pressures and low pressures were applied in the present study. As shown in Fig. 14, the values of $\theta_S$ and $\theta_O$ decrease with increasing pressure in the case of the same S content by comparing Fig. 14(a) and Fig. 14(b). Because the adsorption coefficient was estimated by nitrogen adsorption, further investigations are required to examine the real effects of pressure on the adsorption of S and O. Notwithstanding, when [%S] is 0.0030wt%, the value of $\theta_S$ at the interface in the melts containing 0.03wt% Al is much higher than that of $\theta_O$ according to the thermodynamic results in Fig. 14. Furthermore, with increasing Al content, the fraction of sites covered by S continues to increase, whereas the value of $\theta_O$ simultaneously changes, exhibiting the opposite trend. Clearly, a local high concentration product of Ca and S at the surface of Ca vapor bubbles provided the driving force for the "direct" CaS formation.

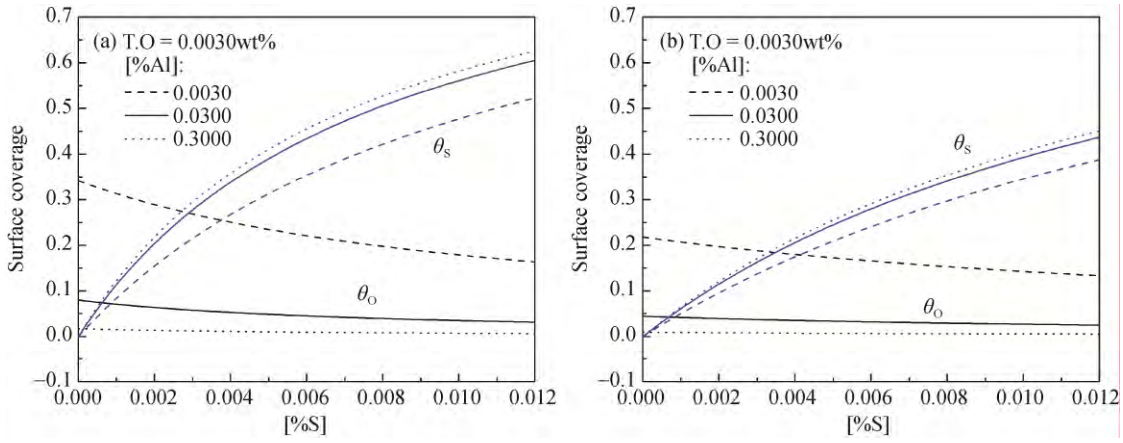


**Fig. 14. Surface segregation of O and S at the interface between the Ca vapor and liquid steel at 1600°C: (a) adsorption coefficient estimated at high pressure; (b) adsorption coefficient estimated at low pressure.**

The transient nature of the CaS phase shortly after Ca treatment is such that they are not thermodynamically stable; thus, because of the reaction between CaS and $Al_2O_3$, this CaS–$Al_2O_3$ duplex inclusion has rarely been observed long after the Ca treatment (in the tundish). The reaction responsible for the Al modification by CaS can be expressed as follows:

$$3(CaS)_{inclusion} + (Al_2O_3)_{inclusion} = 3(CaO)_{inclusion} + 2[Al] + 3[S] \quad (2)$$

Through the aforementioned reaction, both S and Al in the inclusions re-dissolved into the molten steel. Subsequently, the regained $Al_2O_3$ continued to be modified by the newly generated CaO, and a layer of calcium aluminate was formed between the $Al_2O_3$ and CaS. Thus, these discrete particles of CaS in contact with unmodified inclusions were gradually reduced to disappearing levels and $Al_2O_3$ inclusions were ultimately modified into liquid calcium aluminates.

3.2.3. Thermodynamics for CaS shell formation in the tundish

As presented in Figs. 6 and 7, a CaS shell covering liquid calcium aluminate was detected mainly in the tundish. The possible formation mechanism for this shell is that the CaO in the calcium aluminate reacts with Al and S, which can be expressed as follows:

$$3(CaO)_{inclusion} + 2[Al] + 3[S] = 3(CaS)_{inclusion} + (Al_2O_3)_{inclusion} \quad (3)$$

In the present study, the FactSage commercial software was used to characterize the CaO and $Al_2O_3$ activities in calcium aluminates. The limited experimental data obtained by Fujisawa *et al.* [41] and Koroušić [42] are also as presented in Fig. 15 and show no significant differences rela-

tive to the results calculated by FactSage.

As presented in Fig. 15, the well-modified inclusions such as $12CaO{\cdot}7Al_2O_3$ ($C_{12}A_7$) and $3CaO{\cdot}Al_2O_3$ ($C_3A$) exhibit higher CaO activity and lower $Al_2O_3$ activity than $CaO{\cdot}Al_2O_3$ (CA). Thus, the driving force of these liquid inclusions for Eq. (3) to proceed to the right side of the reaction is higher than the driving force of low-modified inclusions. Additionally, the liquid calcium aluminates, relative to the $CaO–Al_2O_3$ inclusions with a high melting temperature, have a higher S capacity [11]. Therefore, the surface of a liquid $xCaO{\cdot}yAl_2O_3$ inclusion provides an advantageous site for CaS formation.

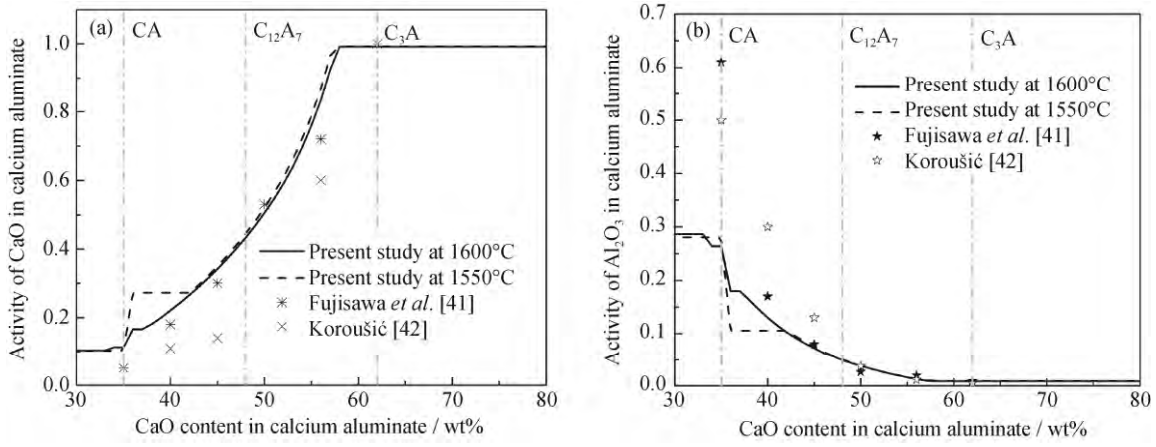


**Fig. 15. Activities of CaO and $Al_2O_3$ in various calcium aluminates estimated with FactSage: (a) activity of CaO in calcium aluminate; (b) activity of $Al_2O_3$ in calcium aluminate.**

Fig. 16 shows the calculated equilibrium relationship between Al and S for the CaS formation at various Ca and O contents in Fe–0.27wt%C–0.3wt%Si–0.45wt%Mn–0.9wt%Cr melt at 1600°C using the FactSage 7.0 software with the FactPS, FToxid, and FTmisc databases. The solid and dashed lines in Fig. 16 represent the zero phase fraction lines of CaS. We interpreted from the thermodynamics analysis that the CaS could be generated on the surface of a liquid calcium aluminate inclusion in the tundish under the current composition conditions, as illustrated in Table 1, in agreement with the SEM results. Furthermore, in the case of [%Ca] = 0.0030wt%, as the O content decreases from 0.0030wt% to 0.0020wt%, the downward shift of the zero phase fraction line of the CaS phase, as shown in Fig. 16, becomes substantial. In turn, a steep decrease in the concentration product of Al and S for CaS generation occurs with the increase of the Ca content, which enhances the risk of generating CaS in the tundish.

3.2.4. Precipitation of CaS during solidification

The primary target of the first Ca treatment in the liquid steel is to modify the inclusions with a high melting point into liquid inclusions, which can subsequently be eliminated during RH refining. Thus, the second Ca addition after RH is designed to increase the retained Ca content in the melts, which is helpful to inhibit the precipitation of MnS inclusion during solidification [28]. To determine the evolutions of the inclusions during solidification of the steel, the inclusion fractions in steels with various Ca and S contents were calculated from 1600 to 1000°C at intervals of 1°C using the FactSage 7.0 software with the FactPS, FToxid, and FSstel databases. The results are presented in Fig. 17.

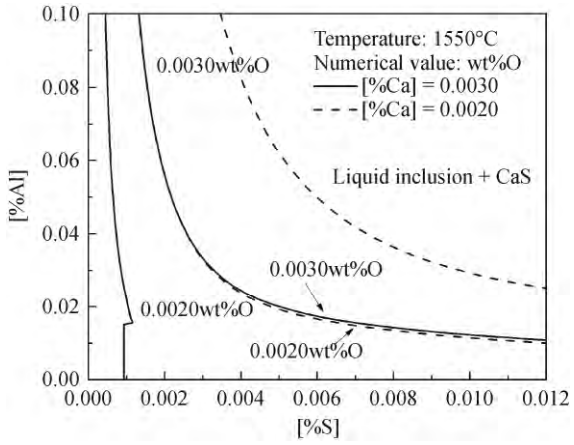


**Fig. 16. Relationship between Al and S for CaS formation in the tundish.**

In Fig. 17(a), dominant inclusions are liquid at 1600°C in the case of [%Ca] = 0.0020wt%. As the temperature decreases from 1600 to 1000°C, the route of the oxide inclusion trajectory was liquid inclusion → $CaO{\cdot}Al_2O_3$ → $CaO{\cdot}2Al_2O_3$ → $CaO{\cdot}6Al_2O_3$ → $Al_2O_3$. The precipitation of CaS starts from the mushy zone temperature and reaches 0.0036wt% at 1000°C, where a small amount of MnS precipitated. With the S content changing to 0.0030wt% (Fig.

17(b)) and 0.0050wt% (Fig. 17(c)), the amount of MnS increases considerably to 0.0037wt% and 0.0091wt%, respectively, whereas no significant changes are observed in the amount of CaS phase. Furthermore, the precipitation temperature of MnS increases with increasing S content according to the calculation results.

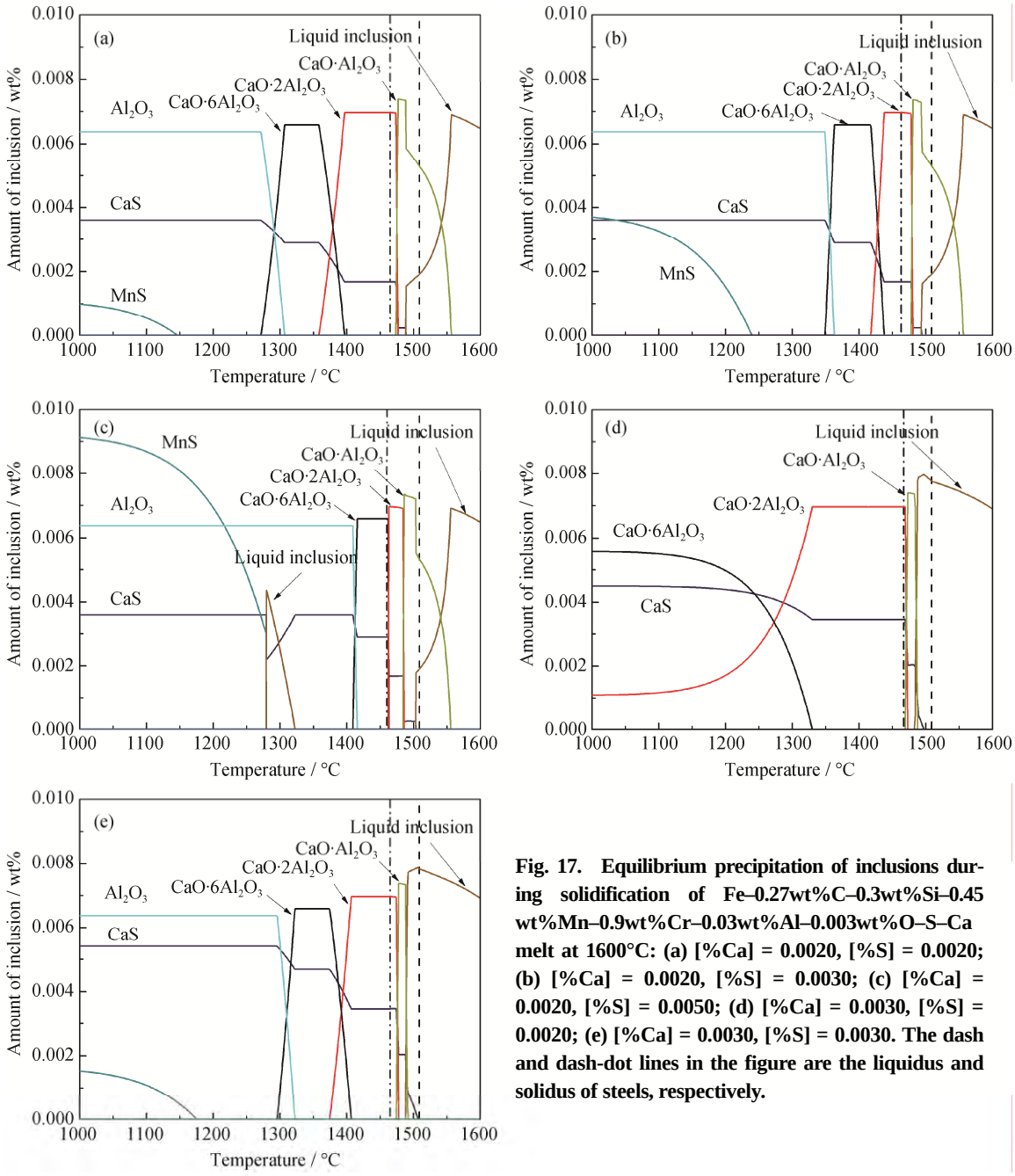


**Fig. 17. Equilibrium precipitation of inclusions during solidification of Fe–0.27wt%C–0.3wt%Si–0.45 wt%Mn–0.9wt%Cr–0.03wt%Al–0.003wt%O–S–Ca melt at 1600°C: (a) [%Ca] = 0.0020, [%S] = 0.0020; (b) [%Ca] = 0.0020, [%S] = 0.0030; (c) [%Ca] = 0.0020, [%S] = 0.0050; (d) [%Ca] = 0.0030, [%S] = 0.0020; (e) [%Ca] = 0.0030, [%S] = 0.0030. The dash and dash-dot lines in the figure are the liquidus and solidus of steels, respectively.**

As presented in Fig. 17(d), when the Ca and S content changes to 0.0030wt% and 0.0020wt%, respectively, the main inclusions remain liquid in the molten steel. Compared with the predicted curves in Fig. 17(a), no MnS was spontaneously produced at 1000°C at the cost of increased CaS inclusions, which could effectively reduce the risk of sulfide stress corrosion cracking. As the S content continues to increase to 0.0030wt% with Ca/S ratio= 1.0 (Fig. 17(e)), MnS inclusions could nevertheless be generated again. Wang *et al.* [43] and Ren *et al.* [24] have recommended that the S content in the steel should be controlled to less than 0.0030wt% to avoid the precipitation of stringer-shaped MnS inclusions. Fortunately, the MnS inclusions could be precipitated at the same level as presented in Fig. 17(a) because of the increase of CaS precipitates. Industrial experiments with Ca treatments of high-strength low-alloy steels by Zhu *et al.* [44]

suggested that the area fraction of MnS would approach zero when the Ca/S ratio is greater than 1 in the tundish. Therefore, not only the S content but also the proportion of Ca to S is important for controlling MnS precipitation during solidification.

### 3.3. Formation mechanism of CaS-bearing inclusions during Ca treatment

On the basis of the preceding analysis, the formation mechanism of CaS-bearing inclusions in the steel is summarized in Fig. 18. First, the CaS particle function as an intermediate reaction product following Ca injection. As depicted in Fig. 18(a), the generation of $Al_2O_3$ inclusion is dominant after the Al wire feeding for deep deoxidation at the Ar-blowing station. When the Si–Ca wire is added into the melt, the CaS forms immediately because of the high surface coverage of S at the surface of Ca vapor bubbles. The initially generated CaS is gradually transformed into CaO through transient reaction between CaS and unmodified $Al_2O_3$ remaining in the steel, whereas the Al and S in the inclusion re-dissolve into the molten steel. Subsequently, the remaining $Al_2O_3$ inclusion is further modified by CaO until the Al inclusion is modified entirely to a liquid calcium aluminate.

CaS can also be precipitated onto the surface of a liquid calcium aluminate inclusion in the tundish, as shown in Fig. 18(b). Moreover, the inner core can be composed of a low-modified $MgO{\cdot}Al_2O_3$ spinel covered with a liquid calcium aluminate. On the basis of the thermodynamic results, at the tundish temperature, the surface of a liquid calcium aluminate with higher CaO activity and lower $Al_2O_3$ activity under appropriate bulk chemical conditions is a favorable site for the generation of the CaS shell.

The third manner is that, during solidification, the CaS can be precipitated directly onto the existing inclusions, as presented in Fig. 18(d). The variety of the existing inclusions results in the various morphologies and structures of the CaS-bearing inclusions observed in the slabs.

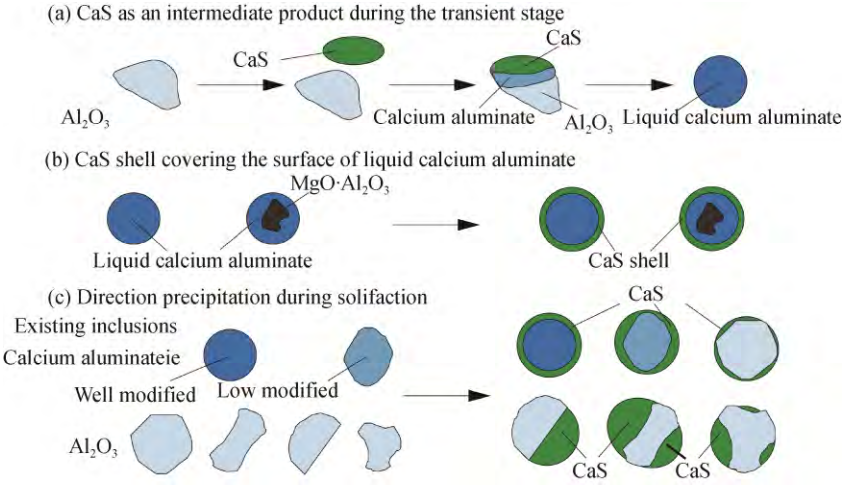


**Fig. 18. Schematic illustration of the mechanisms of formation of various CaS-bearing inclusions: (a) CaS as an intermediate reaction product following Ca treatment; (b) CaS shell surrounding a liquid calcium aluminate in the tundish; (c) CaS directly precipitated on the existing inclusions during solidification of steels.**

## 4. Conclusions

In this manuscript, industrial experiments and thermodynamic calculations were carried out to investigate the evolution and formation of CaS inclusions during double Ca modification. The main conclusions of this study are summarized as follows.

(1) Dual-phase inclusions of CaS–$Al_2O_3$ with an irregular shape were observed shortly after the Ca treatment during 2D and 3D analyses. This type of CaS, as an intermediate reaction product, could modify the $Al_2O_3$ inclusions into liquid calcium aluminates, with the CaS content itself gradually reduced until it disappears. The formation of this type of CaS cannot be predicted from a stability diagram of inclusions calculated using the FactSage software but could be attributed to the high surface coverage of S at the surface of Ca vapor bubbles, which was estimated on the basis of the Langmuir adsorption equation. A simple site coverage model at the interface between the liquid steel and Ca vapor was also established in this manuscript.

(2) The Typical CaS-bearing inclusion that appeared in the tundish was a CaS shell on the surface of a liquid calcium aluminate. This type of CaS exhibited as a ring shape surrounding the inner core during 2D investigations but was

distributed unevenly on the surface of the liquid particle, as revealed by the 3D analysis. The shell of CaS was easily generated on the surface of liquid calcium aluminate with higher CaO activity and greater $Al_2O_3$ activity under the bulk composition condition in the tundish by thermodynamic results.

(3) CaS can also be precipitated directly onto the existing inclusions during solidification of the steel. The variety of the existing inclusions led to the various morphologies and structures of the CaS-bearing inclusions observed in the slabs. Moreover, the precipitation behavior of inclusions during solidification of the steel was also predicted using the FactSage software, which indicated that the S concentration and the Ca/S ratio after the second Ca treatment in the tundish should be critical factors for controlling MnS precipitation during solidification.

## Acknowledgements

This work was financially supported by the National Natural Science Foundation of China (No. 51574026) and we thanks for Pangang Group Co., Ltd. for providing steel samples.

## References

[1] L.F. Zhang and B.G. Thomas, State of the art in the control of inclusions during steel ingot casting, *Metall. Mater.Trans. B*, 37(2006), No. 5, p. 733.

[2] Y.I. Ito, S. Nara, Y. Kato, and M. Suda, Shape control of alumina inclusions by double calcium addition treatment, *Tetsu-to-Hagane*, 93(2007), No. 5, p. 355.

[3] C.F. Dong, K. Xiao, Z.Y. Liu, W.J. Yang, and X.G. Li, Hydrogen induced cracking of X80 pipeline steel, *Int. J. Miner. Metall. Mater.*, 17(2010), No. 5, p. 579.

[4] F.F. Ai, X.L. Xu, Y.Q. Chen, B. Zhong, L. Li, P. Gao, and D.G. Xie, Influence of inclusions on hydrogen induced cracking of oil well pipe steel, *Corros. Prot.*, 33(2012), No. 5, p. 422.

[5] Y.I. Ito, M. Suda, Y. Kato, H. Nakato, and K.I. Sorimachi, Kinetics of shape control of alumina inclusions with calcium treatment in line pipe steel for sour service, *ISIJ Int.*, 36(1996), p. S148.

[6] J.H. Park, S.B. Lee, and D.S. Kim, Inclusion control of ferritic stainless steel by aluminum deoxidation and calcium treatment, *Metall. Mater.Trans. B*, 36(2005), No. 1, p. 67.

[7] J. Guo, S.S. Cheng, H.J. Guo, and Y.G. Mei, Novel mechanism for the modification of $Al_2O_3$-based inclusions in ultra-low carbon Al-killed steel considering the effects of magnesium and calcium, *Int. J. Miner. Metall. Mater.*, 25(2018), No. 3, p. 280.

[8] S.K. Choudhary and A. Ghosh, Thermodynamic evaluation of formation of oxide–sulfide duplex inclusions in steel, *ISIJ Int.*, 48(2008), No. 11, p. 1552.

[9] Y. Miyashita and K. Nishikawa, The deoxidation of liquid iron with calcium, *Tetsu-to-Hagane*, 57(1971), No. 13, p. 1969.

[10] Q.Y. Han, X.D. Zhang, D. Chen, and P.F. Wang, The calcium-phosphorus and the simultaneous calcium–oxygen and calcium–sulfur equilibria in liquid iron, *Metall. Trans. B*, 19(1988), No. 4, p. 617.

[11] S.W. Cho and H. Suito, Assessment of calcium–oxygen equilibrium in liquid iron, *ISIJ Int.*, 34(1994), No. 3, p. 265.

[12] K. Taguchi, H. Ono-Nakazato, D. Nakai, T. Usui, and K. Marukawa, Deoxidation and desulfurization equilibria of liquid iron by calcium, *ISIJ Int.*, 43(2003), No. 11, p. 1705.

[13] K. Tshilombo, Determination of inclusions in liquid steel after calcium treatment, *Int. J. Miner. Metall. Mater.*, 17(2010), No. 1, p. 28.

[14] J.H. Liu, H.J. Wu, Y.P. Bao, and M. Wang, Inclusion variations and calcium treatment optimization in pipeline steel production, *Int. J. Miner. Metall. Mater.*, 18(2011), No. 5, p. 527.

[15] Y. Liu and L.F. Zhang, Relationship between dissolved calcium and total calcium in Al-killed steels after calcium treatment, *Metall. Mater.Trans. B*, 49(2018), No. 4, p. 1624.

[16] G. Ye, P. Jönsson, and T. Lund, Thermodynamics and kinetics of the modification of $Al_2O_3$ inclusions, *ISIJ Int.*, 36(1996), p. S105.

[17] J.M.A. Geldenhuis and P.C. Pistorius, Minimisation of calcium additions to low carbon steel grades, *Ironmaking Steelmaking*, 27(2000), No. 6, p. 442.

[18] G. Xu, Z.H. Jiang, and Y. Li, Formation mechanism of cas-bearing inclusions and the rolling deformation in Al-killed, low-alloy steel with Ca treatment, *Metall. Mater.Trans. B*, 47(2016), No. 4, p. 2411.

[19] K. Kawakami, T. Taniguchi, and K. Nakashima, Generation mechanisms of non-metallic inclusions in high-cleanliness steel, *Tetsu-to-Hagane*, 93(2007), No. 12, p. 743.

[20] S.F. Yang, Q.Q. Wang, L.F. Zhang, J.S. Li, and K. Peaslee, Formation and modification of $MgO{\cdot}Al_2O_3$-based inclusions in alloy steels, *Metall. Mater.Trans. B*, 43(2012), No. 4, p. 731.

[21] Y. Higuchi, M. Numata, S. Fukagawa, and K. Shinme, Inclusion modification by calcium treatment, *ISIJ Int.*, 36(1996), p. S151.

[22] N. Verma, P.C. Pistorius, R.J. Fruehan, M. Potter, M. Lind, and S. Story, Transient inclusion evolution during modification of alumina inclusions by calcium in liquid steel: Part I. Background, experimental techniques and analysis methods, *Metall. Mater.Trans. B*, 42(2011), No. 4, p. 711.

[23] N. Verma, P.C. Pistorius, R.J. Fruehan, M. Potter, M. Lind, and S.R. Story, Transient inclusion evolution during modification of alumina inclusions by calcium in liquid steel: Part II. Results and discussion, *Metall. Mater.Trans. B*, 42(2011), No. 4, p. 720.

[24] Y. Ren, L.F. Zhang, and S.S Li, Transient evolution of inclusions during calcium modification in linepipe steels, *ISIJ Int.*,

54(2014), No. 12, p. 2772.

[25] Y. Ren, Y. Zhang, and L.F. Zhang, A kinetic model for Ca treatment of Al-killed steels using factsage macro processing, *Ironmaking Steelmaking*, 44(2017), No. 7, p. 497.

[26] Y. Liu, L.F. Zhang, Y. Zhang, H.J. Duan, Y. Ren, and W. Yang, Effect of sulfur in steel on transient evolution of inclusions during calcium treatment, *Metall. Mater.Trans. B*, 49(2018), No. 2, p. 610.

[27] A. Ray, S.K. Paul, and S. Jha, Effect of inclusions and microstructural characteristics on the mechanical properties and fracture behavior of a high-strength low-alloy steel, *J. Mater. Eng. Perform.*, 4(1995), No. 6, p. 679.

[28] T. Lis, Modification of oxygen and sulphur snclusions in steel by calcium treatment, *Metalurgija*, 48(2009), No. 2, p. 95.

[29] J. Moon, S.J. Kim, and C. Lee, Role of Ca treatment in hydrogen induced cracking of hot rolled API pipeline steel in acid sour media, *Met. Mater. Int.*, 19(2013), No. 1, p. 45.

[30] L. Holappa, M. Hämäläinen, M. Liukkonen, and M. Lind, Thermodynamic examination of inclusion modification and precipitation from calcium treatment to solidified steel, *Ironmaking Steelmaking*, 30(2003), No. 2, p. 111.

[31] Y. Wang, S. Sridhar, and M. Valdez, Formation of CaS on $Al_2O_3$–CaO inclusions during solidification of steels, *Metall. Mater. Trans. B*, 33(2002), No. 4, p. 625.

[32] J. Guo, S.S Cheng, Z.J. Cheng, and L. Xin, Thermodynamics for precipitation of cas bearing inclusion and their deformation during rolling process for Al-killed Ca-treated steel, *Steel Res. Int.*, 84(2013), No. 6, p. 545.

[33] Y.Y. Bi, A.V. Karasev, and P.G. Jönsson, Evolution of different inclusions during ladle treatment and continuous casting of stainless steel, *ISIJ Int.*, 53(2013), No. 12, p. 2099.

[34] C.W. Bale, P. Chartrand, S.A. Degterov, G. Eriksson, K. Hack, R.B. Mahfoud, J. Melançon, A.D. Pelton, and S. Petersen, FactSage thermochemical software and databases, *Calphad*, 26(2002), No. 2, p. 189.

[35] S. Sun, S. Waterfall, N. Strobl, D. Liao, and D. Holdridge, Inclusion control with Ca treatment to improve castability of low carbon Aluminum-killed steel, [in] *Proceedings of the 8th International Symposium on High-Temperature Metallurgical Processing*, San Diego, 2017, p. 347.

[36] G.R. Belton and R.W. Hunt, How fast can we go? The status of our knowledge of the rates of gas-liquid metal reactions, *Metall. Trans. B*, 24(1993), No. 2, p. 241.

[37] S. Ban-Ya, F. Ishii, Y. Iguchi, and T. Nagasaka, Rate of nitrogen desorption from liquid iron–carbon and iron–chromium alloys with argon, *Metall. Trans. B*, 19(1988), No. 2, p. 233.

[38] K. Harashima, S. Mizoguchi, H. Kajioka, and K. Sakakura, Kinetics of nitrogen desorption from liquid iron with low nitrogen content under reduced pressures, *Tetsu-to-Hagane*, 73(1987), No. 11, p. 1559.

[39] K. Harashima, S. Mizoguchi, M. Matsuo, and A. Kiyose, Rates of nitrogen and carbon removal from liquid iron in low content region under reduced pressures, *ISIJ Int.*, 32(1992), No. 1, p. 111.

[40] T. Harada and D. Janke, Nitrogen desorption from pure iron melts under reduced pressure, *Steel Res. Int.*, 60(1989), No. 8, p. 337.

[41] T. Fujisawa, S. Yamauchiand, and H. Sakao, Activities of CaO and $Al_2O_3$ in CaO–$Al_2O_3$–CaS slags saturated with CaS and the equilibrium between the slags and molten iron alloys at 1873 K, [in] *Proceedings of the 6th International Iron and Steel Congress*, Tokyo, 1990, p. 201.

[42] B. Koroušić, Fundamental thermodynamic aspects of the CaO–$Al_2O_3$–$SiO_2$ system, *Steel Res. Int.*, 62(1991), No. 7, p. 285.

[43] X.H. Wang, X.G. Li, Q. Li, F.X. Huang, H.B. Li, and J. Yang, Control of string shaped non-metallic inclusions of CaS–$Al_2O_3$ system in X80 pipeline steel plates, *Acta Metall. Sin.*, 49(2013), No. 5, p. 553.

[44] T.X. Zhu, M. King, and D. Holdridge, Calcium injection optimization at ArcelorMittal Dofasco Inc.'s LMF 2, [in] *Proceedings of the AISTech 2018*, Philadelphia, 2018, p. 1419.